Geophysical Prospecting

EAGE EUROPEAN ASSOCIATION OF GEOSCIENTISTS & ENGINEERS

Geophysical Prospecting, 2015, **63**, 1086–1096 doi: 10.1111/1365-2478.12204

Image-domain wavefield tomography with extended common-image-point gathers

Tongning Yang[1]* and Paul Sava[2]

[1]*BP America, Houston, TX 77079, USA, and* [2]*Center for Wave Phenomena, Colorado School of Mines, Golden, CO 80401, USA*

Received January 2014, revision accepted August 2014

ABSTRACT

Waveform inversion is a velocity-model-building technique based on full waveforms as the input and seismic wavefields as the information carrier. Conventional waveform inversion is implemented in the data domain. However, similar techniques referred to as image-domain wavefield tomography can be formulated in the image domain and use a seismic image as the input and seismic wavefields as the information carrier. The objective function for the image-domain approach is designed to optimize the coherency of reflections in extended common-image gathers. The function applies a penalty operator to the gathers, thus highlighting image inaccuracies arising from the velocity model error. Minimizing the objective function optimizes the model and improves the image quality. The gradient of the objective function is computed using the adjoint state method in a way similar to that in the analogous data-domain implementation. We propose an image-domain velocity-model building method using extended common-image-point space- and time-lag gathers constructed sparsely at reflections in the image. The gathers are effective in reconstructing the velocity model in complex geologic environments and can be used as an economical replacement for conventional common-image gathers in wave-equation tomography. A test on the Marmousi model illustrates successful updating of the velocity model using common-image-point gathers and resulting improved image quality.

1 INTRODUCTION

Building an accurate and reliable velocity model remains a challenge in current seismic imaging practice. In complex subsurface regions, prestack wave-equation depth migration (e.g., one-way wave-equation migration or reverse-time migration) is a powerful tool for accurately imaging the Earth's interior (Gray *et al.* 2001; Etgen, Gray, and Zhang 2009). Because these migration methods are sensitive to model errors, their widespread use significantly drives the need for high-quality velocity models (Symes 2008; Woodward *et al.* 2008; Virieux and Operto 2009).

Waveform inversion represents a family of techniques for velocity model building using seismic wavefields (Tarantola 1984; Woodward 1992; Pratt 1999; Sirgue and Pratt 2004; Plessix 2006; Vigh and Starr 2008a; Plessix 2009; Symes 2009; Mulder and Leeuwen 2010). This type of methodology, although usually regarded as one of the costliest for velocity estimation, has been gaining momentum in recent years mainly because of its accuracy and advances in computing technology. Usually waveform inversion is implemented in the data domain by adjusting the velocity model such that simulated and recorded data match (Tarantola 1984; Pratt 1999). Such a data match problem often suffers from cycle skipping due to an inaccurate initial model or missing low frequency in the data (Warner *et al.* 2013).

Velocity-model-building methods using seismic wavefields can be implemented in the image domain. Instead of minimizing the data misfit, the techniques in this category update the velocity model by optimizing the image quality. As stated by the semblance principle, the image quality is optimized when the data are migrated with the correct

*E-mail: tongning.yang@bp.com

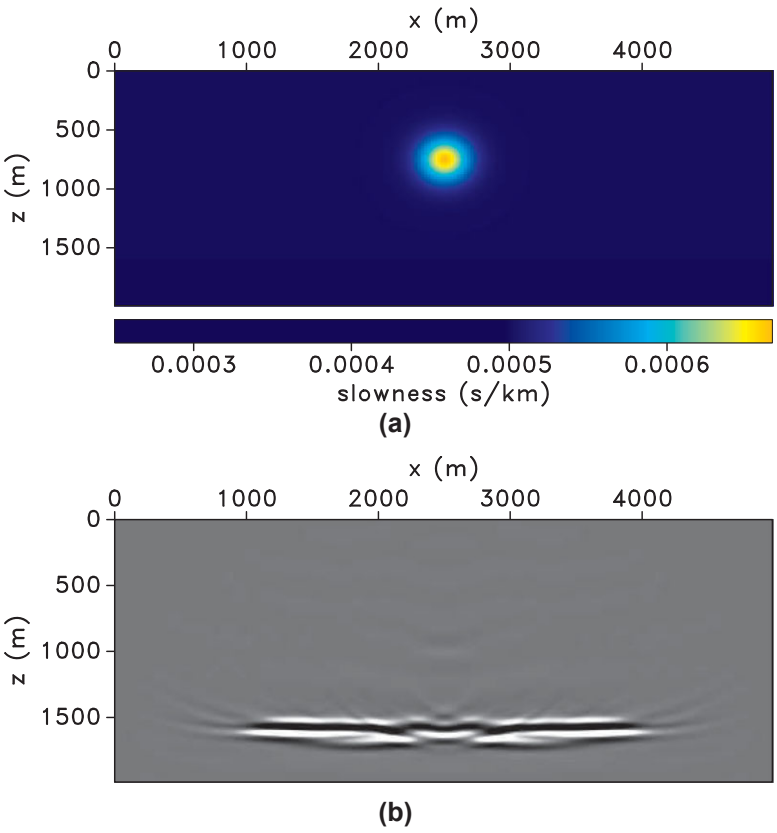

Figure 1 (a) The true slowness model. A horizontal interface at 1.6 km is placed in the density model to generate reflections. (b) The migrated image obtained using the initial constant background model.

velocity model Al-Yahya (1989). The common idea is to optimize the coherency of reflection events in common-image gathers (CIGs) via velocity model updating. These techniques are often referred as image-domain wavefield tomography. Unlike traditional ray-based reflection tomography methods, image-domain wavefield tomography uses band-limited wavefields in the optimization procedure. Thus, this technique is capable of handling complicated wave propagation phenomena such as multi-pathing in the subsurface. In addition, the band-limited character of the wave-equation engine more accurately approximates wave propagation in the subsurface and produces more reliable velocity updates than do ray-based methods.

Wave-equation migration velocity analysis (Sava and Biondi 2004a,b) is one variation of image-domain wavefield tomography. The method linearizes the downward continuation operator and establishes a linear relationship between the model perturbation and image perturbation. The model is inverted by exploiting this linear relationship and minimizing the image perturbation. Differential semblance optimization (DSO) is another variation of image-domain wavefield tomography (Shen and Symes 2008). The idea is to minimize the difference of any given reflection between neighboring offsets or angles by model updates. For DSO, one important element is the choice of the input image gathers. The theory is first introduced based on surface-offset gathers (Symes and Carazzone 1991). The concept is then generalized to space-lag (subsurface-offset) (Shen and Calandra 2005; Shen and Symes 2008). Space-lag gathers have several advantages over other types of gathers. First, space-lag gathers are obtained by wave-equation migration and have fewer artefacts than usually found in surface-offset gathers obtained by Kirchhoff migration, and thus, they are suitable for velocity analysis in complex subsurface targets (Stolk and Symes 2004). Second, the implementation using space-lag gathers is automatic in a way that no moveout picking is required, which significantly reduced human interference. Recent progress includes the extension of these methods to using reverse-time migration (Weibull et al., 2013; Shan and Wang, 2013) and to anisotropic media (Li et al., 2012; Weibull and Arntsen, 2014).

In practice, however, the use of space-lag gathers is limited by the computation and storage requirements. In 3D, space-lag gathers need to compute the lags in both inline and crossline directions. This leads to 5D image hypercubes that

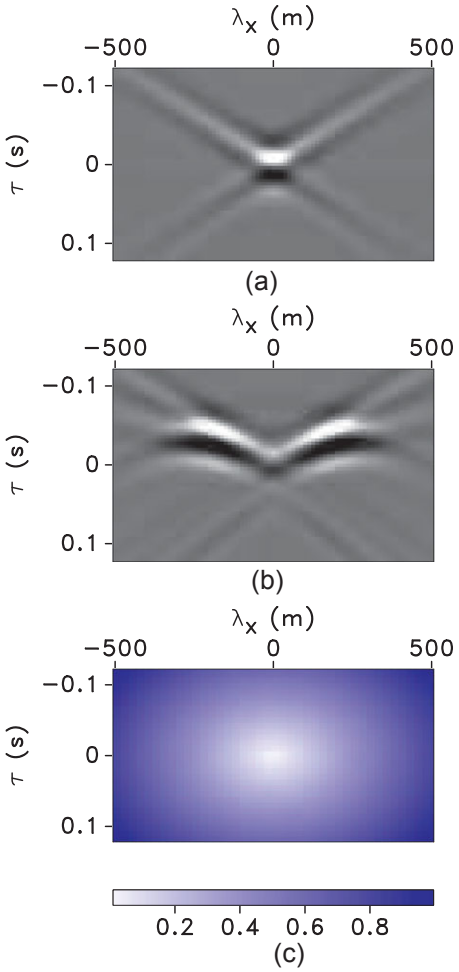

Figure 2 Common-image-point gathers sampled at the middle of the reflector for (a) the true model and (b) the initial model. (c) The penalty operator applied to the CIPs.

are too expensive to compute and store. Clapp (2007) proposed using field-programmable gate arrays to accelerate the space-lag gathers construction. Compressed sensing can also be used to reduce computation and storage cost, as proposed by Zhang, Biondi, and Clapp (2013). To overcome the issues of space-lag gathers, we propose to use common-image-point gathers (CIPs) as an alternative to space-lag gathers for image-domain wavefield tomography. The discrete sampling of the point gathers provides a flexible way to extract the velocity information from the image and facilitates target-oriented velocity updates. Furthermore, the sparse construction of the gathers reduces computational cost and storage requirements, which are both are important in 3D applications. Other practical aspects regarding computational cost for image-domain wavefield tomography fall outside the scope of this paper, e.g., I/O issue (Fei and Williamson 2010).

We start this paper by introducing CIPs with focus on how to choose the gather locations. We then discuss the theory of image-domain wavefield tomography and its implementation with CIPs. Next, we introduce illumination weighting for the gathers aimed at improving the robustness of the method. We use the Marmousi model to demonstrate that wavefield tomography using CIPs offers a more economical alternative than conventional approach using space-lag gathers for model building in complex subsurface areas.

2 THEORY

For clarity, we separate the theory section into three parts. We first discuss the picking algorithm to sample common-image-point gathers in the subsurface. We then explain the gradient computation for image-domain wavefield tomography using CIPs. A synthetic example will be used to illustrate the flow as well. In the third part, we explain the construction of the illumination-based weighting function, which is used to improve the robustness of the inversion.

2.1 Gathers locations picking

The essential and key characteristic of CIPs is the sparse sampling of gathers along reflections in the subsurface. In contrast, space-lag gathers used in conventional approach are sampled in the whole subsurface. This full sampling of the gathers substantially increases the cost and may degrade the gathers if they are sampled on noise or artefacts. The sampling locations for CIPs are determined using an image-guided automatic algorithm (Cullison and Sava 2011). The algorithm first computes the image planarity, structure-oriented semblance, and the amplitude envelope; then use the multiplication of these three measures as the priority map to guide the location picking. The priority map ensures that the gathers are sampled on coherent and continuous reflection events in the subsurface. In such a way, we achieve a robust characterization of the velocity information from the images. The sparsity of the gathers construction is enforced by using exclusion zones. The exclusion zones can be generated using structure tensor, and the size of the zones is user defined. The actual gathers' location is selected using a greedy heuristic picking method in the order of priority map value.

2.2 Gradient computation

For the image-domain wavefield tomography method discussed here, the objective function is formulated by applying the idea of DSO to CIPs. The gradient is computed by applying the adjoint state method (Plessix 2006; Symes 2009),

For simplicity, we discuss the derivation in the frequency domain. We formulate the inverse problem by first defining the state variables, through which the objective function is related to the model parameters. The state variables for our problem are the source and receiver wavefields u_s and u_r obtained by solving the following acoustic wave equation:

$$\begin{bmatrix} \mathcal{L}(x,w,m) & 0 \\ 0 & \mathcal{L}^*(x,w,m) \end{bmatrix} \begin{bmatrix} u_s(j,x,w) \\ u_r(j,x,w) \end{bmatrix} = \begin{bmatrix} f_s(j,x,w) \\ f_r(j,x,w) \end{bmatrix}, \tag{1}$$

where f_s is the source function; f_r are the recorded data; $j = 1, \cdots N_s$, where N_s is the number of shots; ω is the angular frequency; and $\mathbf{x} = \{x, y, z\}$ are the space coordinates. The wave operator $\mathcal{L}$ and its adjoint $\mathcal{L}^*$ propagate the wavefields forward and backward in time, respectively, using either a one-way or two-way wave equation. In this formulation, we designate operator $\mathcal{L}$ to be

$$\mathcal{L} = -\omega^2 m - \Delta, \tag{2}$$

where Δ is the Laplace operator, and m represents slowness squared.

Figure 1(a) shows the synthetic model used to illustrate the flow. The true model consists of a Gaussian low-velocity anomaly in a constant background. A contrast at 1.6 km in the density model is used to generate the reflections. The initial model is the constant background, and the corresponding migrated image is shown in Fig. 1(b). The imaged reflection is distorted due to the missing anomaly in the initial model.

In the second step of the adjoint state method, we first construct the objective function. Then, the adjoint sources are derived based on the objective function and used to model the adjoint state variables. As the objective function measures the image incoherency caused by model error, minimizing the objective function simultaneously reconstructs the model and improves the image quality. The objective function for DSO is defined as:

$$\mathcal{H}_\lambda = \frac{1}{2} \| P(\lambda) r(x,\lambda) \|^2_{x,\lambda}, \tag{3}$$

where

$$r(\mathbf{x},\lambda) = \sum_j \sum_\omega \overline{u_s(j,\mathbf{x}-\lambda,\omega)} u_r(j,\mathbf{x}+\lambda,\omega) \tag{4}$$

the overline represents complex conjugate, and

$$P(\lambda) = |\lambda|. \tag{5}$$

The penalty operator annihilates the focused energy at zero lags and highlights the defocusing at non-zero lags.

For CIPs, Sava and Vasconcelos (2011) analyze the kinematic characteristics of reflections and point out that reflections focus at zero space and time lags when the migration velocity is correct. This feature is similar to that of space-lag gathers used in DSO. Therefore, we can define a DSO-type objective function for CIPs as

$$\mathcal{H}_{\lambda,\tau} = \frac{1}{2} \| P(\lambda,\tau) r(\mathbf{c},\lambda,\tau) \|^2_{\mathbf{x},\lambda,\tau}, \tag{6}$$

where $r(\mathbf{c},\lambda,\tau)$ are CIPs sampled on locations $\mathbf{c}$ picked using the algorithm described in the previous section:

$$r(\mathbf{c},\lambda,\tau) = \sum_j \sum_\omega \overline{u_s(j,\mathbf{c}-\lambda,\omega)} u_r(j,\mathbf{c}+\lambda,\omega) \, \mathrm{e}^{2i\omega\tau}. \tag{7}$$

$P(\lambda,\tau)$ is expressed as follows:

$$P(\lambda,\tau) = \sqrt{|\lambda|^2 + (V\tau)^2}, \tag{8}$$

where the space-lag vector $\lambda = \{\lambda_x, \lambda_y, 0\}$, and V is a constant scalar. Figure 2(a) and Fig. 2(b) show two CIPs constructed in the middle of the reflector (Fig. 1(b)) for true and initial models, respectively. The energy is focused in the gathers for the true model and vice versa for the initial model. The penalty operator is shown in Fig. 2(c).

Given $\mathcal{H}_{\lambda,\tau}$ in equation (6), the adjoint sources are computed as objective function's derivatives with respect to the state variables u_s and u_r. To facilitate the derivation, we introduce an operator T that represents the space shift applied to the wavefields and is defined as

$$T(\lambda) u(j,\mathbf{x},\omega) = u(j,\mathbf{x}+\lambda,\omega). \tag{9}$$

Thus, adjoint sources g_s and g_r are

$$\begin{aligned} g_s(j,\mathrm{x},w) &= \sum_{\lambda,\tau} T(\lambda) P(\lambda,\tau) \overline{P(\lambda,\tau) r(\mathbf{x},\lambda,\tau)} \\ &\quad \times T(\lambda) u_r(j,\mathbf{x},\omega) \, \mathrm{e}^{-2i\omega\tau} \\ g_r(j,\mathrm{x},w) &= \sum_{\lambda,\tau} T(-\lambda) P(\lambda,\tau) \overline{P(\lambda,\tau)} r(\mathbf{x},\lambda,\tau) \\ &\quad \times T(-\lambda) u_s(j,\mathbf{x},\omega) \, \mathrm{e}^{-2i\omega\tau}. \end{aligned} \tag{10}$$

Adjoint state variables a_s and a_r are the wavefields obtained by backward and forward modeling, respectively, using the corresponding adjoint sources defined in equation (10):

$$\begin{bmatrix} \mathcal{L}^*(\mathrm{x},w,m) & 0 \\ 0 & \mathcal{L}(\mathrm{x},w,m) \end{bmatrix} \begin{bmatrix} a_s(j,\mathrm{x},w) \\ a_r(j,\mathrm{x},w) \end{bmatrix} = \begin{bmatrix} g_s(j,\mathrm{x},w) \\ g_r(j,\mathrm{x},w) \end{bmatrix}, \tag{11}$$

and $\mathcal{L}$ and $\mathcal{L}^*$ are the same wave propagation operators used in equation (1).

The last step of the gradient computation is simply the correlation between state variables and adjoint state variables:

$$\frac{\partial \mathcal{H}_{\lambda,\tau}}{\partial m} = \sum_j \sum_\omega \frac{\partial \mathcal{L}}{\partial m}(u_s(j,\mathrm{x},w)\overline{a_s(j,\mathrm{x},w)} + u_r(j,\mathrm{x},w)\overline{a_r(j,\mathrm{x},w)}), \tag{12}$$

where $\frac{\partial \mathcal{L}}{\partial m}$ is the partial derivative of the wave propagation operator with respect to the model parameter. Using the definition of $\mathcal{L}$ in equation (2), we find that $\frac{\partial \mathcal{L}}{\partial m}$ is simply $-\omega^2$. Figure 3(a) shows a gradient for one CIP in the middle and computed from one shot at 1.5 km. The two branches correspond to the source- and receiver-side cross-correlations of the state and adjoint state variables. The gradient for all CIPs and all shots stacked is shown in Fig. 3(b), which characterizes the Gaussian anomaly.

The derivation above shows the construction of objective function and gradient for image-domain wavefield tomography. Given these two components, the solution to the inverse problem is found by minimizing the objective function using non-linear gradient-based iterative methods. In each iteration, the gradient is computed and the model update is calculated by line search in the steepest descent or conjugate gradient directions (Vigh and Starr 2008b). Using this flow, the updated model after ten iterations for the synthetic test is shown in Fig. 4(a), where the Gaussian anomaly is accurately reconstructed. The migrated image using the updated model is plotted in Fig. 4(b), where the image quality is improved.

2.3 Illumination weighting

The objective function $\mathcal{H}_{\lambda,\tau}$ defined in equation (6) is minimized when the reflections focus at zero lag, an indication of the correct velocity model. This, however, occurs only when the subsurface is well illuminated and the data have sufficient spatial sampling. Otherwise, imbalanced illumination or irregular acquisition geometry can result in defocusing in the gathers even if the velocity model is correct (Yang, Shragge and Sava, 2012). To mitigate the negative influence of the uneven subsurface illumination, we can employ a weighting function such that the gathers in poor-illumination areas are down-weighted as the defocusing information is less reliable than for the gathers in good-illumination areas. Such a weighting function stabilizes the inversion and improves the robustness of the model building process.

The weighting function is constructed using the illumination analysis. Illumination analysis in the framework of wave-equation migration is formulated using the solution to migration deconvolution problems (Yu and Schuster 2003). Migration deconvolution first establishes a linear relationship between a reflectivity distribution $\tilde{r}$ and seismic data d:

$$\mathcal{M}\tilde{r}\,(\mathbf{x}) = d, \tag{13}$$

where $\mathcal{M}$ represents a forward Born modeling operator that is linear with respect to the reflectivity. A migrated image is obtained by applying the adjoint of the modeling operator $\mathcal{M}^*$ to the data,

$$\mathcal{M}^* d = \mathcal{M}^*\mathcal{M}\tilde{r}\,(\mathbf{x}) = r\,(\mathbf{x})\,, \tag{14}$$

where r is a migrated image. Note that the migrated image is the result of blurring the reflectivity $\tilde{r}$ by $(\mathcal{M}^*\mathcal{M})$. $(\mathcal{M}^*\mathcal{M})$ is the Gauss–Newton approximation to the Hessian of the least squares misfit function, and it includes the subsurface illumination information associated with the velocity structure and acquisition geometry. In practice, matrix $(\mathcal{M}^*\mathcal{M})^{-1}$ is effectively non-invertible, but its impact can be evaluated by applying a cascade of demigration and migration operator $(\mathcal{M}^*\mathcal{M})$ to an image:

$$r_I\,(\mathbf{x}) = \mathcal{M}^*\mathcal{M}r\,(\mathbf{x}). \tag{15}$$

The quotient $r_I\,(\mathbf{x})\,/r\,(\mathbf{x})$ approximates the diagonal elements of the Hessian and characterizes the illumination effects. This quotient is used as the illumination weighting function for our method. The weighting function is calculated using the initial velocity model. Although the model will be updated during the inversion, we assume that the illumination is a slowly varying function with respect to the model changes. As a result, the same illumination weighting is used to precondition the gathers throughout the inversion.

3 EXAMPLES

In this section, we illustrate our method with synthetic Marmousi example to show its ability to reconstruct velocity models in complex subsurface regions.

The correct model is shown in Fig. 5(a). The source locations are evenly distributed on the surface from 1.0 km to 7.0 km at a spacing of 0.1 km. The receiver arrays are fixed for all the shots and span entirely the surface at a spacing of 0.01 km. The data are generated via finite-difference Born modeling using a Ricker wavelet with a peak frequency of 15 Hz. The data are then transformed into the frequency domain because both the migration and wavefield tomography

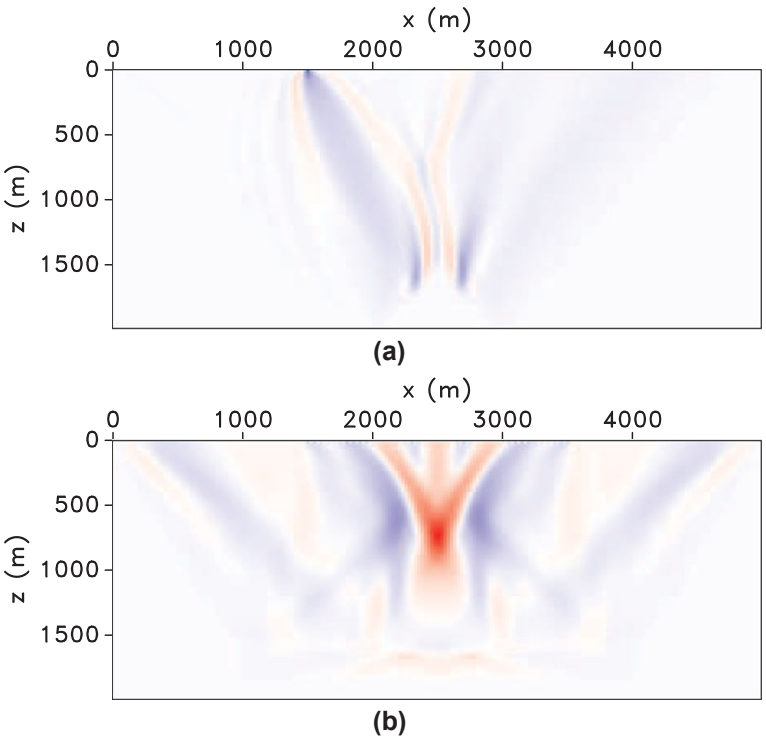

Figure 3 Gradient for (a) one shot located at 1.5 km and (b) all shots.

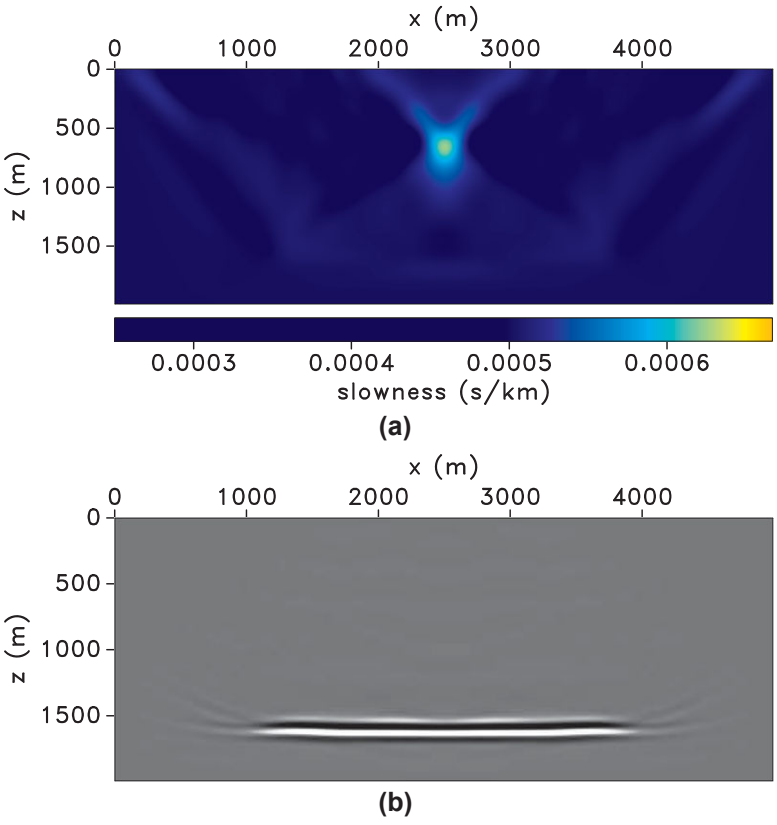

Figure 4 (a) The updated model after ten iterations of inversion using CIPs. (b) The migrated image obtained using the updated model.

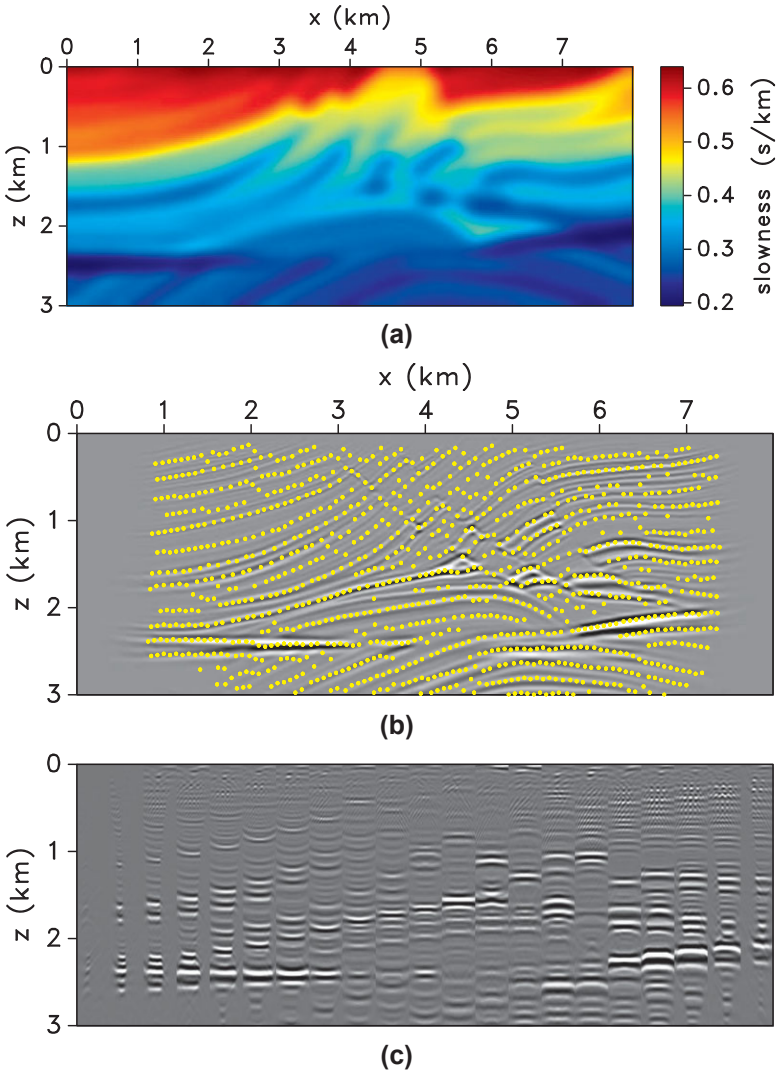

Figure 5 (a) The true model used to generate the data. (b) The migrated image overlain with the CIPs' location. (c) The angle-domain gathers obtained using the true model.

operators are based on the frequency-domain downward continuation method. In this way, we avoid using the same operator for both the modeling and inversion procedures. The image and angle gathers migrated with the true model are shown in Fig. 5(b) and (c). As one might expect, reflection events in the angle gathers are flat because the correct model is used for migration. The initial model used for the inversion, Fig. 6(a), is a highly smoothed version of the true model. This model resembles the results one can obtain from conventional ray-based reflection tomography. Fig. 6(b) and (c) shows the image and angle-domain CIGs migrated with the initial model. Since the initial model is highly smoothed, it lacks the necessary components required by the migration to produce an accurate result. Thus, the migrated image exhibits distortions in the reservoir region around $x = 5$ km $z = 2.5$ km. The reduced image quality can be further confirmed by the residual moveout in the angle gathers, as shown in Fig. 6(c). In our example, the angle gathers are used only for quality control not for the model building.

We initiate our velocity analysis process by selecting CIPs' gather locations at which we construct extended images necessary for velocity analysis. These locations are selected using the automatic picking algorithm developed by Cullison and Sava (2011) as we discuss in the prevous theory section. Figure 6(b) shows the picked locations overlain on the image. They follow the coherent structure of the image and tend to be randomly positioned where the reflections are less coherent. Figure 7 shows the weighting function obtained using equation (15). We apply it to the input gathers in order to compensate for the uneven illumination effects in the subsurface. Light colors

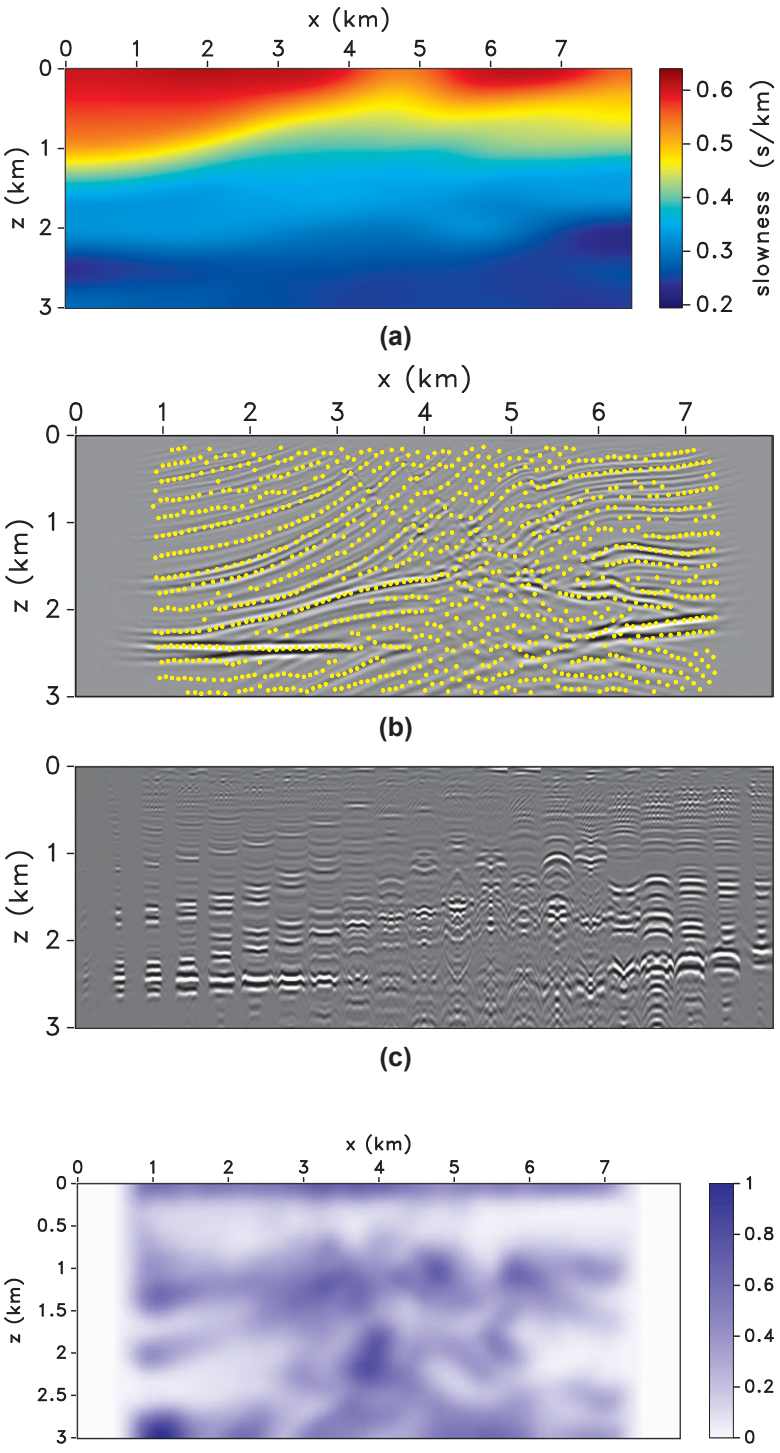

Figure 6 (a) The initial model used in the velocity inversion. (b) The migrated image overlain with the CIPs' location. (c) The angle-domain gathers obtained using the initial model.

Figure 7 The weighting function based on the subsurface illumination.

indicate low values of the weights, which correspond to the poor-illumination areas, and dark colors indicate high values of the weights, which correspond to the good-illumination areas. This weighting function downweights the gathers in the poor-illumination areas such that the inversion suffers less from the unreliable information. Fig. 8(a) and (b) shows the inverted model after 20 nonlinear iterations and the corresponding migrated image. The updated model improves the

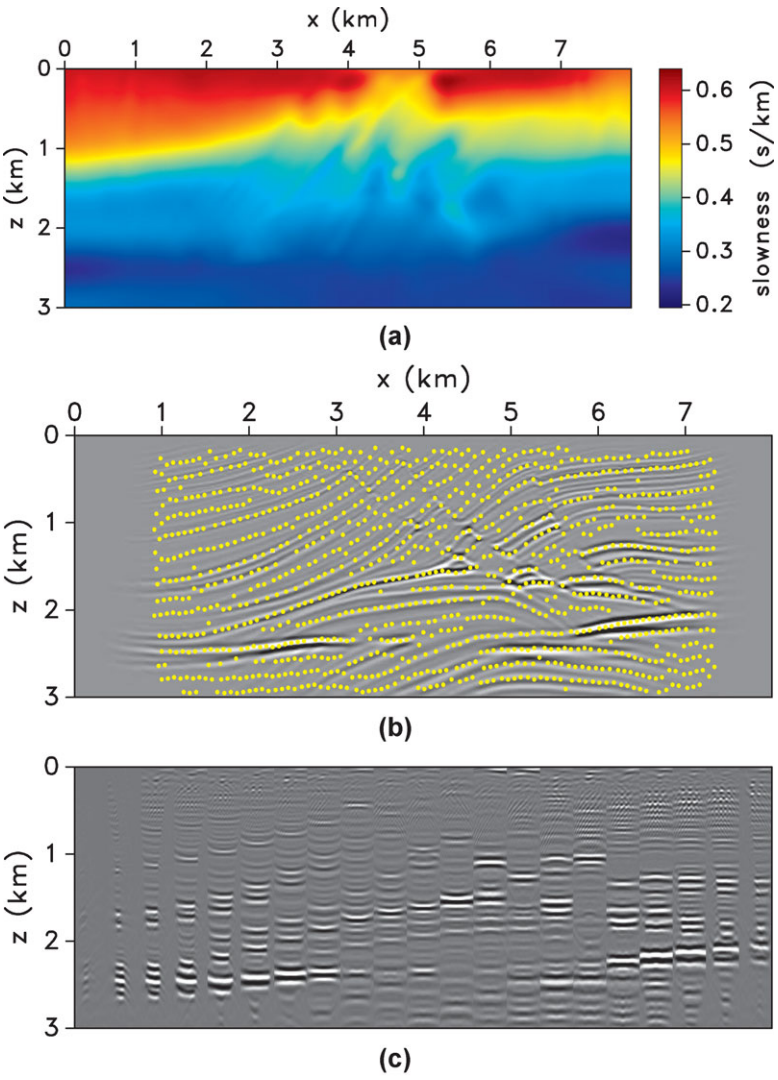

Figure 8 (a) The updated model after 20 iterations of inversion using CIPs. (b) The migrated image overlain with the CIPs' locations. (c) The angle-domain gathers obtained using the updated model.

imaging quality in the area ranges from $x = 4 \sim 6.5$ km and from $z = 1 \sim 3$ km as the reservoir is better focused and more coherent now. In addition, the reflections are flatter in angle gathers, as shown in Fig. 8(c), as compared with those in Fig. 6(c). These also indicate the improvement of the image due to the model updates.

4 DISCUSSION

The synthetic examples demonstrate the velocity model updates produced using common-image-point gathers. After running the inversion, the main features of the model are resolved and they help improve the quality of the image. The improvements can be directly observed from the more coherent image and flatter events in angle gathers. In either case, CIPs are sparsely sampled along the reflectors but they are still able to capture the velocity error and reconstruct the model. Compared to conventional Differential semblance optimization approach using space-lag gathers, the computation and storage cost for gathers is smaller. For space-lag gathers, the cost is proportional to the size of the model and number of lags we compute: $C \sim N_x N_y N_z N_{\lambda_x} N_{\lambda_y}$. For CIPs, the cost is proportional to the number of points and lags we compute: $C \sim N_c N_{\lambda_x} N_{\lambda_y} N_\tau$. Here N_c denotes the number of CIPs. Notice that the cost reduction is determined by the ratio $N_c N_\tau / (N_x N_y N_z)$. The number of time lags N_c is usually a small window, which is only required to accommodate the wavelet. Thus the ratio of N_τ / N_z is generally less than 0.1. The ratio of $N_c / (N_x N_y)$ may depend on the complexity of the subsurface. Given the complex model like Marmousi model, we can still achieve the satisfied result using point gathers less

than 1% of the total grid points. Another advantage of CIPs is that the gathers are always sampled on reflections as the picking is done using the greedy algorithm applied to the priority map. This improves the robustness of the gathers compared with space-lag gathers because the gathers suffer less from the noise or artefacts in the image.

5 CONCLUSIONS

We have demonstrated a wavefield-based velocity-model-building method implemented in the image domain. The procedure optimizes the velocity model by minimizing the image incoherency caused by model errors. The objective function is designed for common-image-point gathers constructed sparsely on the reflection event. The penalty operator used in the objective function is aimed at improving the focusing of the reflections in the gathers.

The synthetic examples demonstrate that CIPs are able to characterize velocity error from focusing of the energy in the gathers, and the wavefield tomography converts the information into accurate velocity updates. The main advantage of using CIPs over conventional space-lag gathers in the wavefield tomography approach is that using CIPs reduce the cost for computing and storing the input image gathers while still producing reliable and accurate model updates. This is mainly attributed to the optimized sampling of CIPs in the subsurface as only the significant reflections are analyzed to provide information for velocity update. The illumination-based weighting helps improve the stability and robustness of the inversion in complex subsurface areas.

ACKNOWLEDGEMENTS

We acknowledge the support of the sponsors of the Center for Wave Phenomena at Colorado School of Mines. We would also like to thank the editor Felix Herrmann, and three anonymous reviewers for their constructive comments and suggestions. This research was supported in part by the Golden Energy Computing Organization at the Colorado School of Mines using resources acquired with financial assistance from the National Science Foundation and the National Renewable Energy Laboratory.

REFERENCES

Al-Yahya K. 1989. Velocity analysis by iterative profile migration. *Geophysics* **54**, 718–729.

Clapp R. 2007. Accelerating subsurface offset gathers for 3D seismic applications using FPGAs. 77th SEG annual international meeting, Expanded Abstracts, 2383–2387.

Cullison T. and Sava P. 2011. An image-guided method for automatically picking common-image-point gathers. 81st SEG annual international meeting, Expanded Abstracts.

Etgen J., Gray S.H. and Zhang Y. 2009. An overview of depth imaging in exploration geophysics. *Geophysics* **74**, WCA5–WCA17.

Fei W. and Williamson P. 2010. Overcoming the I/O bottleneck of adjoint state method based migration velocity analysis. 80th SEG annual international meeting, Expanded Abstracts, 4057–4061.

Gray S.H., Etgen J., Dellinger J. and Whitmore D. 2001. Seismic migration problems and solutions. *Geophysics* **66**, 1622–1640.

Li Y., Shen P. and Perkins C. 2012. Vti migration velocity analysis using rtm. Presented at the 81th Annual International Meeting, SEG, Expanded Abstracts.

Mulder W.A. and Leeuwen T.V. 2010. A correlation-based misfit criterion for wave-equation traveltime tomography. *Geophysical Journal International* **182**, 1383–1394.

Plessix R.-E. 2006. A review of the adjoint state method for computing the gradient of a functional with geophysical applications. *Geophysical Journal International* 167, 495–503.

Plessix R.-E. 2009. Three-dimensional frequency-domain full-waveform inversion with an iterative solver. *Geophysics* **74**, WCC53–WCC61.

Pratt R.G. 1999. Seismic waveform inversion in the frequency domain, Part 1: Theory and verification in a physical scale model. *Geophysics* **64**, 888–901.

Sava P. and Biondi B. 2004a. Wave-equation migration velocity analysis - I: Theory. *Geophysical Prospecting* **52**, 593–606.

Sava P. and Biondi B. 2004b. Wave-equation migration velocity analysis - II: Subsalt imaging examples. *Geophysical Prospecting* **52**, 607–623.

Sava P. and Vasconcelos I. 2011. Extended imaging condition for wave-equation migration. *Geophysical Prospecting* **59**, 35–55.

Shan G. and Wang Y. 2013. Rtm based wave-equation migration velocity analysis. 83th Annual International Meeting, SEG, Expanded Abstracts, 4726–4731.

Shen P. and Calandra H. 2005. One-way waveform inversion within the framework of adjoint state differential migration. 75th SEG annual international meeting, Expanded Abstracts, 1709–1712.

Shen P. and Symes W.W. 2008. Automatic velocity analysis via shot profile migration. *Geophysics* **73**, VE49–VE59.

Sirgue L. and Pratt R. 2004. Efficient waveform inversion and imaging: A strategy for selecting temporal frequencies. *Geophysics* **69**, 231–248.

Stolk C.C. and Symes W.W. 2004. Kinematic artifacts in prestack depth migration. *Geophysics*, **69**, 562–575.

Symes W. 2009. Migration velocity analysis and waveform inversion. *Geophysical Prospecting* **56**, 765–790.

Symes W.W. 2008. Migration velocity analysis and waveform inversion. *Geophysical Prospecting* **56**, 765–790.

Symes W.W. and Carazzone J.J. 1991. Velocity inversion by differential semblance optimization. *Geophysics* **56**, 654–663.

Tarantola A. 1984. Inversion of seismic reflection data in the acoustic approximation. *Geophysics* **49**, 1259–1266.

Vigh D. and Starr E.W. 2008a. 3D prestack plane-wave, full-waveform inversion. *Geophysics* **73**, VE135–VE144.

Vigh D. and Starr E.W. 2008b. Comparisons for waveform inversion, time domain or frequency domain?. 78th SEG annual international meeting, Expanded Abstracts, 1890–1894.

Virieux J. and Operto S. 2009. An overview of full-waveform inversion in exploration geophysics. *Geophysics* **74**, WCC1–WCC26.

Warner M., Ratcliffe A., Nangoo T., Morgan J., Umpleby A., Shah N., et al. 2013. Anisotropic 3D full-waveform inversion. *Geophysics* **78**, R59–R80.

Weibull W. and Arntsen B. 2014. Anisotropic migration velocity analysis using reverse-time migration. *Geophysics* **79**, R13–R25.

Weibull W., Arntsen B., Houbiers M. and Mispel J. 2013. Automatic anisotropic migration velocity analysis for reverse time migration. Presented at the 82th Annual International Meeting, SEG, Expanded Abstracts.

Woodward M., Nichols D., Zdraveva O., Whitfield P. and Johns T. 2008. A decade of tomography. *Geophysics* **73**, VE5–VE11.

Woodward M.J. 1992. Wave-equation tomography. *Geophysics* **57**, 15–26.

Yang T., Shragge J. and Sava P. 2012. Illumination compensation for image-domain wavefield tomography. 74th annual international meeting, Abstracts, European Association of Exploration Geophysicists.

Yu J. and Schuster T. 2003. Migration deconvolution vs. least squares migration. 74th SEG annual international meeting, Expanded Abstracts.

Zhang Y., Biondi B. and Clapp R. 2013. Accelerating residual move-out based wave-equation migration velocity analysis with compressed sensing. 83th SEG annual international meeting, Expanded Abstracts, 4744–4749.